INVESTIGATION OF DIFFERENT INITIAL ORBIT DETERMINATION METHODS FOR RADAR BEAM-PARK EXPERIMENTS

M. Budoni[(1)], C. Carloni[(1)], D. Cerutti-Maori[(1)], I.O. Maouloud[(1)], J. Rosebrock[(1)], S. Lemmens[(2)], and J. Siminski[(2)]

[(1)]*Fraunhofer Institute for High Frequency Physics and Radar Techniques FHR, Fraunhoferstraße 20, 53343 Wachtberg, Germany, Email: matteo.budoni@fhr.fraunhofer.de*
[(2)]*European Space Agency - European Space Operations Centre (ESA - ESOC), Robert-Bosch-Straße 5, 64293 Darmstadt, Germany*

ABSTRACT

The huge number of unknown space debris infesting the near-Earth orbits represents a serious menace for the life of active satellites. For the purposes of spacecraft safety, it is extremely important to characterize and catalog as many debris as possible. Radar Beam-Park Experiments (BPEs) allow to get insights into the space debris statistical distribution. By applying adapted Initial Orbit Determination (IOD) techniques to the data collected during a BPE, it is possible to associate a preliminary orbit estimate with each detected object. The accuracy of these techniques needs to be investigated to assess the benefit of such estimations. To perform this investigation, a BPE was simulated and the output data were processed via different IOD methods. This paper presents and discusses the results of the simulation, focusing on the comparison of the performance of the considered IOD techniques.

Keywords: Space Debris; Radar Beam-Park Experiment; Initial Orbit Determination.

1. INTRODUCTION

The number of space debris orbiting the Earth is continuously growing and is considerably larger than the number of operational satellites. The space debris population poses a severe threat to the operations of active satellites, because as it grows in number, the probability of in-orbit debris-satellite collisions increases as well. Such collisions have the potential to destroy the satellite and even to trigger the so-called Kessler effect [1], compromising the usability of all the involved orbital regions. As a consequence, to ensure the safeguarding of current and future space missions, it is of absolute importance to get insights into the distribution of these objects. Two major models have been developed to describe the space debris population: ESA's Meteoroid and Space Debris Terrestrial Environment Reference model (MASTER) and NASA's Orbital Debris Engineering Model (ORDEM). Currently, according to the ESA Space Debris User Portal [2], about 28210 debris objects are regularly tracked by space surveillance networks and maintained in their catalog. This is, however, only a small fraction of the tremendously high number of debris orbiting the Earth. Indeed, the statistical models estimate that there are around 34000 debris greater than 10 cm, 900000 debris between 1 cm and 10 cm and 128 millions debris between 1 mm and 1 cm [2].

Radars and telescopes are the primary sensors used to track and catalog the space debris. Specifically, radar systems are employed to observe the Low Earth Orbit (LEO) region, while for larger ranges the optical telescopes are preferable. In order to calibrate and verify the space debris population models, observation campaigns are regularly coordinated by the Inter-Agency Space Debris Coordination Committee (IADC). One type of these campaigns consists in the realization of the so-called Beam-Park Experiments (BPEs), mainly conducted with radar systems. In such experiments, the radar antenna is 'parked' looking towards a certain direction and data are collected continuously for around 24 hours.

The Fraunhofer Institute for High Frequency Physics and Radar Techniques (Fraunhofer FHR) participates in BPE campaigns since 1993 with its Tracking and Imaging Radar (TIRA). The TIRA system, sketched in Fig. 1, has a 34 m parabolic antenna and is equipped with two different radars: an L-band tracking radar and a Ku-band imaging radar (not used during a BPE) [3].

After a BPE, Fraunhofer FHR provides a detection list that includes several parameters for the observed objects such as the range, the range rate, the Radar Cross Section (RCS), the diameter (obtained using the NASA Size Estimation Model [4]), the altitude and the Doppler inclination [5]. There are however some limitations. The Doppler inclination is obtained under the assumption of circular orbit. Therefore, for objects on eccentric orbits, this parameter is poorly estimated because the adopted model is no longer valid. Additionally, the Doppler inclination is derived from a second order equation with two admissible solutions that lead to an ambiguity for beam pointing directions other than East or West [5].

It could be beneficial for calibrating the space debris pop-

ulation models to include in the detection list also the full orbital state of the detected objects, e.g., in the form of the six Keplerian orbital elements. In order to assess the benefits of such an addition, we need to understand whether these parameters can be reliably estimated, or at least bounded, from BPE data by using adapted Initial Orbit Determination (IOD) methods. We need as well to investigate the expected accuracy of these different IOD techniques. A straightforward upside is that these methods do not resort to the limiting assumption of circular orbit. A downside is that the IOD solution accuracy is limited by the low amount of information contained in the very short orbit arcs observed (typical time intervals for BPE observations are in the order of few seconds).
In this paper, we examine the performance of several IOD techniques and compare their accuracy. To achieve this goal, we simulated a 10-day East-staring BPE performed with the TIRA system, by using the in-house developed 'SpaceView' software. The parameters of the simulation (i.e., antenna beam, waveform, etc.) were selected identical to those of the TIRA system L-band radar. By applying a geometrical filter, we reproduced the list of all the objects crossing the antenna beam and simulated, for each pass, all the associated observation vectors measured by the radar. Then, we added to these measurements white Gaussian-distributed noises, computed according to different values of the Signal to Noise Ratio (SNR). Finally, we processed these data through the selected IOD methods. We used both state-of-the-art techniques and newly developed techniques derived at Fraunhofer FHR. Following this methodology, we investigated the quality of the estimated orbits for the different IOD methods, as well as for the different input SNR values.
It must be noted that the IOD performances presented in this paper correspond, actually, to an upper bound. Indeed, in this simulation, we kept the SNR constant over each individual pass and we neglected the RCS variations from pulse to pulse as well as the antenna pattern modulation. However, these effects occur with real observations and, moreover, the phase of the object complex reflectivity is not constant over time. All these features cause a decorrelation of the radar data, a variation of the estimated parameter accuracy along the same pass and, eventually, discontinuities in the target detection over time. Thus, in a real BPE investigation, all these factors would have a negative impact on the IOD performances.
The structure of the paper is the following: Section 2 describes the BPE simulation. Section 3 introduces the different examined IOD techniques. Section 4 presents and discusses the results of the analysis. Lastly, Section 5 concludes the investigation.

2. SIMULATION

This section describes the BPE simulation. The first part of this simulation is similar to the one presented in [6].

The in-house software 'SpaceView' was used to realize a BPE that spanned a time interval of 10 days (13.12.2019-23.12.2019). Such a long duration was chosen in order to

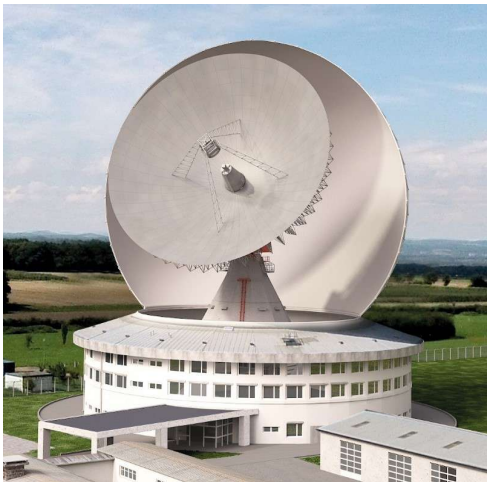

Figure 1. TIRA system sketch.

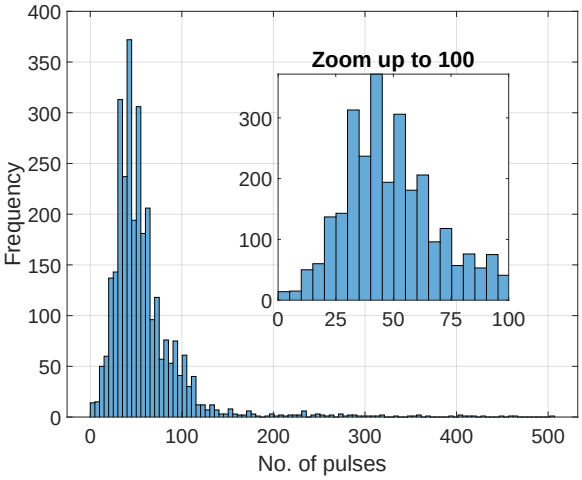

Figure 2. Frequency distribution of the number of pulses for the 3018 simulated beam crossings. On the top right, there is a zoom of the first part of the distribution (up to a number of pulses equal to 100).

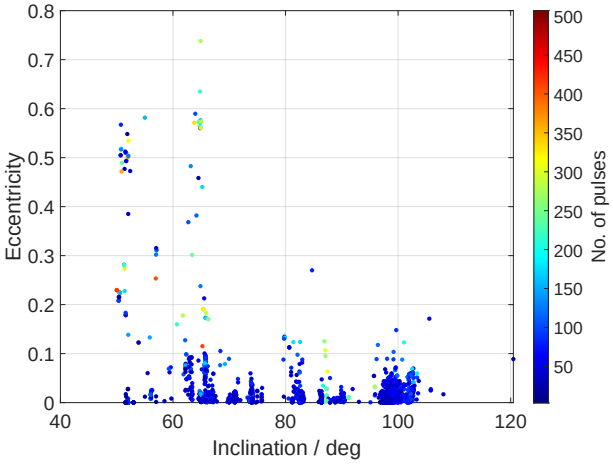

Figure 3. Orbital parameters of inclination and eccentricity for the 3018 simulated beam crossings. The associated number of pulses is indicated in the colorbar.

have a larger number of beam crossing objects, leading to more statistically significant parameter distributions for the simulated passes. Concerning the beam pointing direction, an East-staring configuration was selected. Hence, the antenna was 'parked' towards East with an azimuth angle of 90° and an elevation angle of 75°. The antenna beam-width was set to 0.5°, (i.e., approximately the 3 dB beam-width of the TIRA L-band radar) while the range window was included between a lower bound of 300 km and an upper bound of 5000 km.

The software 'SpaceView' took as input the whole satellite catalog downloaded from the SpaceTrack web page [7] on the 12th of December 2019. By that time, the catalog included the Two Line Element sets (TLE) of 18628 objects (both active and inactive), spread around the different orbit regimes of LEO, Medium Earth Orbits (MEO), Geostationary Earth Orbits (GEO) and Highly Elliptical Orbits (HEO). 'SpaceView' propagated all the TLEs for the entire simulation time span by using the simplified perturbation model SGP4 [8]. Then, through the application of a simple geometrical filter, it recorded the list of all the objects crossing the antenna beam. It is important to mention that this list was obtained without recurring to any radar performance model to compute the detection probability (i.e., we assumed that all the objects crossing the beam were detected by the radar).

After some minor pre-processing steps, aimed at maximizing the number of beam crossings as well as the number of associated pulses, we obtained 3018 visible passes in the simulation, belonging to 2709 different objects. The frequency distribution of the number of pulses for all these beam crossings is shown in Figure 2. Figure 3, instead, presents, for each pass, the orbital parameters of inclination and eccentricity, included in the TLE of the corresponding space object, together with the related number of pulses (indicated in the colorbar).

In addition to the list of all the crossing objects (with the associated TLE orbital parameters), for each beam crossing, 'SpaceView' produced as output a list of several time-dependent parameters. These parameters, described in Table 1, were provided every 0.033 s, i.e., with a sampling frequency of 30 Hz, comparable to the Pulse Repetition Frequency (PRF) of the TIRA system. In this list, we have the time stamp associated with each pulse (from which we can compute the total beam crossing time) as well as the radar observables of range, range rate, azimuth and elevation. Another listed parameter is the range rate rate. This latter is the second temporal derivative of the range and, currently, is not provided by the TIRA system, but could be derived through a dedicated coherent signal processing [9]. The beam crossing list also contains the satellite position and velocity vectors in the Earth Centered Inertial (ECI) reference frame, obtained from the TLE through the SGP4 propagation. These vectors represent the reference data used to assess the performance of the different IOD methods.

For every pass, we added white Gaussian-distributed noises to the four radar measurements of range, range rate, azimuth and elevation to replicate the effects of a real observation. The noises we introduced, had zero mean and a standard deviation dependent on the value of the SNR. We assumed that the SNR was constant along all the passes. For the noise addition, we considered seven different SNR values (from 0 dB to 30 dB, with increments of 5 dB). As a result, we obtained seven different noisy data sets for each of the 3018 beam crossings. Such data sets were fed to the selected IOD techniques, presented in the next section.

Table 1. List of the time-dependent output parameters obtained by 'SpaceView' software for each beam crossing. ECI stands for Earth Centered Inertial reference frame.

Parameter	Symbol	Unit
Time	t	s
Range	R	m
Range rate	RR	m/s
Range rate rate	$RR2$	m/s^2
Azimuth angle	Az	deg
Elevation angle	El	deg
Position in ECI	P_{ECI}	km
Velocity in ECI	V_{ECI}	km/s

3. IOD TECHNIQUES

In this section, we briefly describe the six IOD techniques selected for the current analysis. Out of these six methods, two are state-of-the-art techniques, well known and established in the literature. The other four have been recently developed at Fraunhofer FHR [10].

The first technique under evaluation is described in [11]. From the name of the authors of this manuscript, we called this method the 'Kaiser-Jehn' method, or briefly KJ. This algorithm was already successfully tested in the past with real beam-park data coming from the TIRA system. For this reason, we selected it as a reference method for this paper. In KJ, a weighted linear fit is performed on the measurements of range rate, azimuth and elevation. A linear trend is assumed as well for the range, with the central point set equal to its mean value. The newly obtained observation vectors are then exploited to compute two position vectors spaced in time by 1 s. Lastly, from their differential quotient, a velocity vector is estimated.

The other state-of-the-art technique is the worldwide used Herrick-Gibbs algorithm [12], here referred to as HG. HG requires as input three co-planar sequential position vectors to determine the orbit. HG is a variation of the Gibbs method [13], specifically used when the position vectors are very close to each other, that is exactly the case we have with BPE data. HG uses a Taylor-series expansion to estimate the velocity vector corresponding to the central position vector. The satellite dynamics assumed by HG follows the two-body problem (only the gravitational force of the Earth is considered).

The third analyzed algorithm is a generalization of HG

and is therefore abbreviated as HGG. Instead of considering only three position vectors, HGG uses as input all the position vectors we manage to estimate from the pass data, i.e., as many as the number of measured observation vectors. As output, this method finds the position and velocity vectors associated with the central time, by solving the final system of equations in a least squares sense. With HGG, the J2 perturbation is also included in the satellite dynamics.
The next IOD technique is another generalization of HG, that, additionally, takes into account the range rate information provided by the TIRA system. We refer to this method as HGGRR. As previously with HGG, HGGRR includes the J2 perturbation in the satellite dynamics and exploits all the estimated position vectors. Also this algorithm solves the final system in a least squares sense to find the central position and velocity vectors. In contrast with HGG, here, the final system has an entire set of new equations coming from the definition of the range rate, i.e., the satellite velocity vector projected along the line of sight.
The fifth method under analysis is the two-body integrals IOD, or simply TB. As its name suggests, this method assumes that the satellite follows the dynamics of the two-body problem, without taking into consideration any perturbation force. TB exploits the conservation of two quantities that remain invariant along the orbit of a spacecraft with such dynamics: the angular momentum vector per unit of mass and the energy per unit of mass. By equating these two quantities evaluated at two different time instants, we obtain a system of equations that is solved to estimate the two corresponding velocity vectors. This approach is already present in the literature. It was first proposed in [14] and then revisited e.g., in [15, 16, 17, 18]. Since for this method only two observation vectors are required, we tried to improve their accuracy by merging together the information contained in several adjacent pulses. We performed an averaging on a number of pulses varying on a case by case basis, according to each individual pass length, but with an upper limit fixed to 31 pulses (i.e., with a maximum time distance between the first and the last considered pulses of 1 s). Thanks to this averaging, we achieved observation vectors less affected by the noise [19].
The last technique considered for this investigation exploits the estimation of the range rate rate, parameter already introduced in Section 2. Knowing this parameter, indeed, the velocity vector of the space object can be fully determined. Since the range rate rate is derived through a coherent signal processing, we refer to this algorithm as coherent integration IOD, or briefly CI. In CI, the satellite dynamics includes also the J2 perturbation.
For HG, HGG, HGGRR and TB, we studied two different realizations: the first one uses as input the noisy measurements as they come from the simulation; the second one, instead, performs beforehand the same fit on the measurements realized in KJ in order to smooth out the oscillations introduced by the noise. The algorithms with the fit are referred to as HGf, HGGf, HGGRRf and TBf, respectively.

4. RESULTS

This section presents the results of the paper. It is divided into two parts. Section 4.1 compares the performance of the different IOD methods, considering a minimum visibility time threshold of 0.5 s. Section 4.2 investigates how the number of pulses associated with each beam crossing affects the IOD accuracy.

4.1. IOD performance investigation

As described in Section 2, we have 3018 beam crossings for each of the seven considered SNR values. For the analysis concerning the IOD performances, we decided to discard all the beam crossings with a duration below 0.5 s, i.e., with a number of associated pulses lower than 15. In those cases, indeed, even a single outlier caused by the noise would have the potential to compromise the IOD solution. By introducing this step, we removed a few passes, reducing their number from 3018 to 2960. The observation vectors associated with the remaining beam crossings were processed with the IOD techniques described in Section 3.
After the application of each IOD method, we obtained for each crossing object as output a state vector (position and velocity) in the ECI reference frame. Such state vector was compared with the corresponding position and velocity vectors derived from the TLE through the SGP4 propagation. A first measure of the accuracy of the IOD techniques can be given in terms of differences between these vectors. Specifically, we computed two residuals: the norm of the position vector difference and the norm of the velocity vector difference. For each SNR and each algorithm, we obtained 2960 residuals for the position and 2960 for the velocity. We calculated the mean values of these two residuals and plotted them in Figure 4 and Figure 5.
Figure 4(a) shows the mean of the position residuals against the SNR for all the selected IOD methods. It is clearly visible that the algorithms that do not perform an initial fit on the noisy measurements lead to less accurate results, especially with low SNR values, i.e., with higher noises. TB without the fit leads instead to results comparable to TBf, since, by averaging together several adjacent pulses, we already filtered out partially the effects of the noise.
Figure 4(b) is a zoom of Figure 4(a) in which the non-fitted algorithms are left out. We can see that CI is the IOD technique that performs best, having the highest improvement in particular with low values of the SNR. This enhancement is caused by the coherent signal processing performed on the radar data, that is more complex than the simple data fitting used by the other methods. The CI residuals range from 2 km with an SNR of 0 dB to 65 m at 30 dB. On the other hand, all the other algorithms reach almost exactly the same level of accuracy (from 2.3 km at 0 dB to 75 m at 30 dB). Indeed, their computation of the position vector follows very similar mathematical steps.
For the velocity, this uniform behavior is lost since each

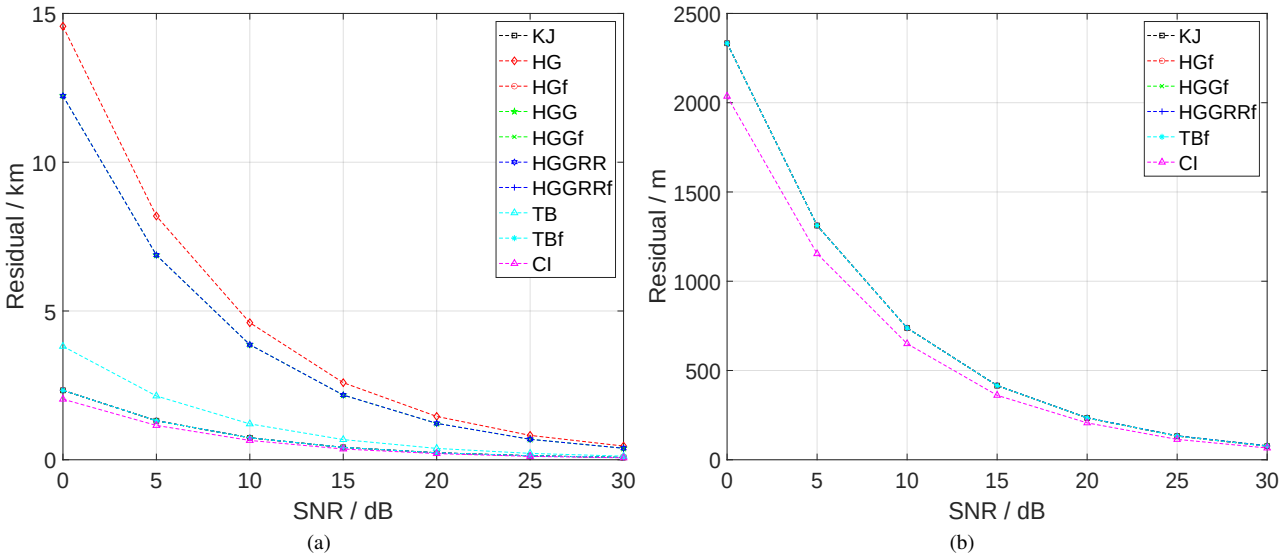

Figure 4. Mean of the norm of the position vector difference against the SNR. The figure on the left presents the residuals in km *for all the IOD techniques. The figure on the right shows the residuals in* m *for the coherent integration IOD and all the algorithms that perform the fit on the measurements.*

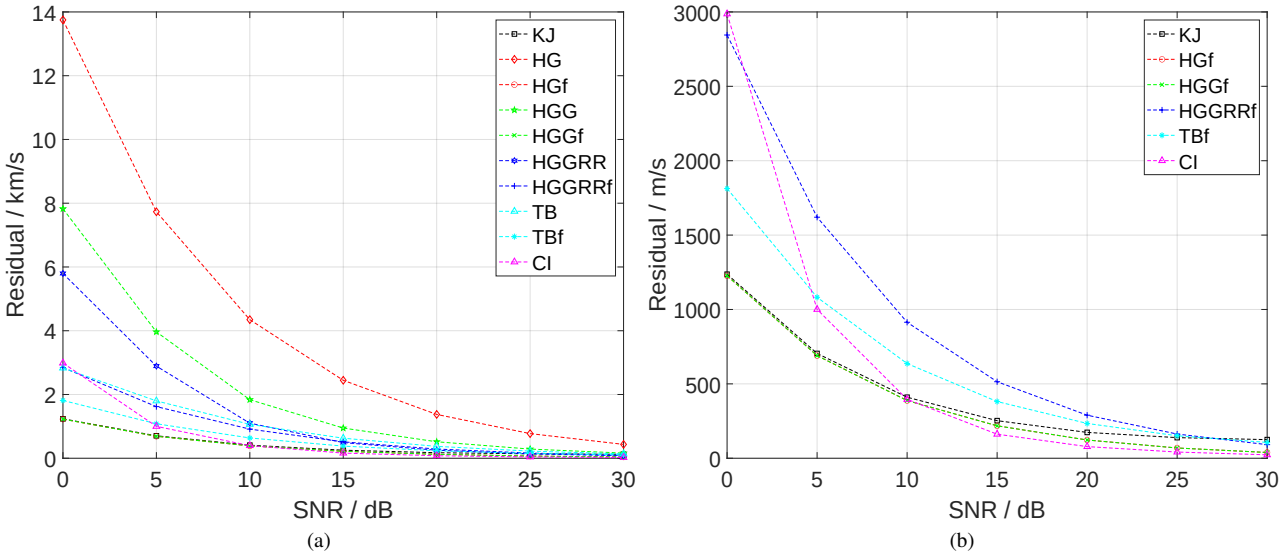

Figure 5. Mean of the norm of the velocity vector difference against the SNR. The figure on the left presents the residuals in km/s *for all the IOD techniques. The figure on the right shows the residuals in* m/s *for the coherent integration IOD and all the algorithms that perform the fit on the measurements.*

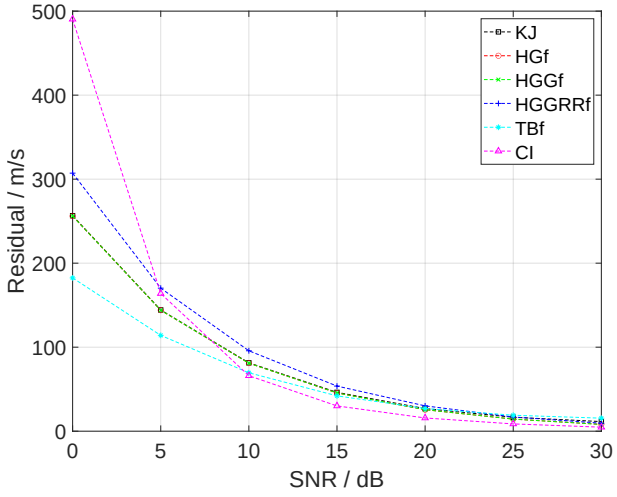

(a) Radial component

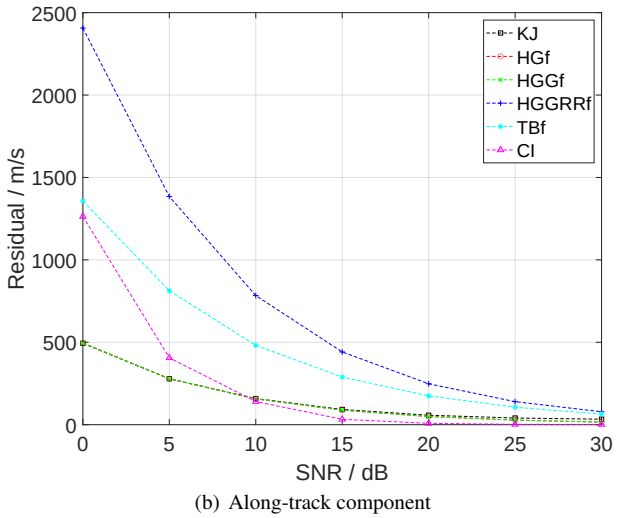

(b) Along-track component

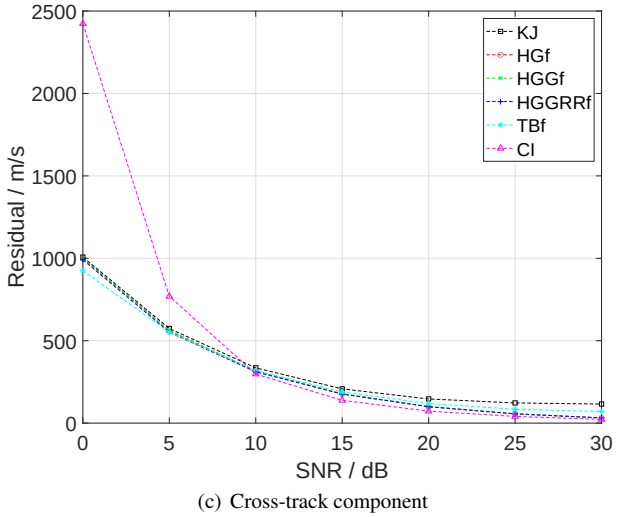

(c) Cross-track component

Figure 6. Means of the absolute values of the three velocity vector difference components along the coordinate axes of the RSW reference frame. The plots present the residuals in m/s *against the SNR for the coherent integration IOD and all the algorithms that perform the fit on the measurements. The top, mid and bottom figures show the residuals along the radial, along-track and cross-track components, respectively.*

algorithm follows very different procedures to estimate this quantity. Figure 5(a) shows, for all the different IOD techniques, the mean of the velocity residuals against the SNR. We notice again that the algorithms that take as input the noisy measurements without the fit lead to less accurate results, but this time, excluding HG, the difference is not that wide. We even have the unexpected result that, for SNR higher than 15 dB, HGGRR performs slightly better than its corresponding HGGRRf (this unexpected result needs to be investigated in more detail).

The zoom leaving out the algorithms without the fit, is shown in Figure 5(b). In this case, there is a higher variability between the techniques, with only two algorithms overlapping: HGf and HGGf. In contrast with what happens with the position residuals, for the velocity, there is not a method performing always better. For very low SNR values, HGf and HGGf lead to the highest accuracy (1.2 km/s with an SNR of 0 dB and 700 m/s at 5 dB). With an SNR of 10 dB, their performances are matched by CI as well (residuals around 400 m/s). Finally, from an SNR of 15 dB on, CI gives the best results (ranging from 160 m/s at 15 dB to 20 m/s at 30 dB).

For the velocity vector, in addition to the norm of the difference, we present also other three residuals. By exploiting the state vector obtained from the TLE propagated with SGP4, we found for each beam crossing the corresponding transformation matrix to rotate the vectors from the ECI reference frame into the RSW coordinate system. This latter system, defined in [20], is widely used to describe satellite relative displacements, so it fits perfectly for such analysis. Its coordinate axes are the radial direction (parallel to the ECI position vector), the along-track direction (perpendicular to the ECI position vector) and the cross-track direction (normal to the plane defined by the ECI position and velocity vectors).

We applied this rotation to both the velocity vectors, i.e., the one derived from the TLE and the output of the different IOD techniques. Then, for each method and each SNR value, we computed the difference between the two rotated vectors and we used the absolute values of the three resulting components as residuals for the investigation.

The mean values of these residuals are shown in Figure 6 against the SNR for the coherent integration IOD and all the algorithms that perform the fit on the measurements. From the figures, it is again possible to notice how HGf and HGGf overlap.

For the radial residuals, we see in Figure 6(a) that at low SNR values, TBf is the method giving the highest accuracy (180 m/s at 0 dB and 115 m/s at 5 dB) with a quite considerable distance with respect to the other techniques. From 10 dB on, instead, CI allows to reach the best results (from 65 m/s at 10 dB to 5 m/s at 30 dB). At higher SNR values, however, the accuracy of all the methods is pretty similar.

Figure 6(b) shows that, for the along-track component, CI is again the preferable algorithm from an SNR of 10 dB on, with an accuracy ranging from 140 m/s at 10 dB to 1.5 m/s at 30 dB. Only in correspondence with an SNR of 0 dB and 5 dB, this result is overturned by HGf, HGGf and KJ (accuracy around 500 m/s and 280 m/s, respectively).

Lastly, for the cross-track component, we can see in Figure 6(c) that TBf gives the best accuracy for small SNR values (around 925 m/s at 0 dB and 550 m/s at 5 dB), where CI has notably larger residuals compared to all the other techniques. From 10 dB on, however, CI becomes once more the most accurate algorithm (accuracy going from 300 m/s at 10 dB to 20 m/s at 30 dB).
If we analyze each technique individually with respect to the mean residuals for the three different velocity components, we see that the behavior of the various algorithms is different. Independently of the SNR values, KJ, HGf and HGGf have the cross-track residual always larger than the along-track, with the radial being the smallest. The same behavior is valid for CI as well up to an SNR of 15 dB, while, from 20 dB, the along-track becomes the lowest residual. Finally, for HGGRRf and TBf, the along-track residual is the most significant, followed by the cross-track and lastly by the radial (with only one exception at 30 dB where for TBf the cross-track is larger).
When trying to characterize a spacecraft, we can not neglect talking about its orbital parameters. Therefore, the final analysis presented in this section concerns the orbital parameters of semi-major axis, eccentricity, inclination and true longitude. This latter quantity is the sum of the right ascension of the ascending node, the argument of the periapsis and the true anomaly. We used the true longitude instead of considering the three angles individually, to avoid the problems of orbital singularity rising when the inclination or the eccentricity are null or too close to zero.
For this investigation, we computed the osculating orbital elements from the state vectors obtained through the different IOD techniques. Then, we compared these quantities with the corresponding osculating elements derived from the SGP4 propagated state vectors. The absolute values of the differences represent our residuals. For each SNR value and each IOD method, we calculated the median of such residuals. We used the median for this analysis in order to avoid the effects of the outliers corrupting the mean value.
Table 2, Table 3, Table 4 and Table 5 present the results of this investigation for the coherent integration IOD and all the algorithms that perform the initial fit on the measurements. Once more, in all the tables, it is possible to see that the accuracy obtained with HGf and HGGf is almost identical.
Table 2 shows the semi-major axis residuals. CI, with an accuracy ranging from 323.9 km at 0 dB to 2.1 km at 30 dB, is performing considerably better than all the other algorithms. With the exception of 0 dB, there is always a factor bounded within 7 and 13 between the residuals of CI and the finest of the other algorithms.
The eccentricity residuals are listed in Table 3. For an SNR of 0 dB, KJ, HGf and HGGf perform best, with a residual of 0.0841. From an SNR of 5 dB, instead, CI gives the most accurate results (residuals from 0.0153 at 5 dB to 0.0004 at 30 dB). In this case, the difference with respect to the performance of the other algorithms is not as large as for the semi-major axis (without considering the SNR of 0 dB, the gain factor is always included between 3 and 7).
For the inclination residuals, shown in Table 4, at 0 dB, TBf has the lowest median (3.20°), at 5 dB, KJ, HGf, HGGf and HGGRRf have the highest accuracy (1.81°) and from 10 dB on, CI becomes once more the preferable algorithm (residuals from 0.91° at 10 dB to 0.07° at 30 dB). For this parameter, the advantage of using CI (when it is performing better) is not that evident (we have a gain factor slightly larger than 1, with a maximum around 1.4).
Table 5 presents the residuals for the true longitude. With low SNR values, HGf and HGGf are the algorithms performing best (with an accuracy of 3.98° at 0 dB and 2.24° at 5 dB), while again, from 10 dB on, CI overturns this result (residuals from 1.14° at 10 dB to 0.09° at 30 dB). As for the inclination, also for the true longitude, when CI is performing better, its accuracy is comparable to that of the other algorithms (the gain factor is always included between a little more than 1 and 1.4).

4.2. Impact of the number of pulses

In the previous section, we applied a threshold on the minimum visibility time of 0.5 s, corresponding to a minimum number of 15 pulses within each beam crossing. We justified this choice by saying that with too few pulses, even a single outlier originated by the noise would have the potential to corrupt the IOD solution. By introducing this condition, we lost 48 of the 3018 simulated beam crossings.
However, the selected IOD methods work even with less than 15 pulses. Specifically, KJ and TB requires a minimum of two observation vectors, whereas HGG, HGGRR and CI a minimum of three. On the other hand, HG needs as input exactly three sets of measurements. When performing the fit on the radar observables, though, the higher the number of pulses, the more statistically reliable the final solution becomes. Indeed, in such cases, an equal number of outliers would degrade less significantly the resulting fit accuracy.
We present in this section the performance of the IOD methods in terms of velocity vector residuals, with respect to the number of pulses associated to each beam crossing. For the sake of completeness, in this analysis, we considered also the beam crossings with a number of pulses below 15. We fixed the SNR at 15 dB and we computed the norm of the velocity vector differences between the output of the different IOD techniques and the TLE propagation. Then, we created clusters of beam crossings according to their associated number of pulses. We grouped together all the passes with a number of pulses included in the interval 1-5, 6-10 and so on with a fixed increment of 5, up to 510, i.e., the maximum value obtained in the simulation. Within each cluster, we computed the mean of the velocity vector residuals and we plotted the results on a bar graph.
Figure 7 shows these plots for the coherent integration IOD and all the algorithms that perform the initial fit on the measurements. These figures have an upper limit of 50 pulses on the x-axis, since we wanted to focus mainly on the passes with only few pulses. Moreover, we observed that, from that value, the curves reach approxi-

Table 2. Median of the semi-major axis residuals. The table lists the results in km *against the SNR for the coherent integration IOD and all the algorithms that perform the fit on the measurements.*

	0 dB	5 dB	10 dB	15 dB	20 dB	25 dB	30 dB
KJ	636.7	362.6	210.3	125.1	82.3	63.3	59.7
HGf	646.1	367.6	207.1	114.0	64.7	36.8	21.1
HGGf	645.5	366.4	206.4	114.9	64.5	36.4	20.5
HGGRRf	2772.3	1859.9	1118.3	639.9	359.5	203.2	113.9
TBf	1697.1	1081.5	673.8	420.1	254.6	152.8	92.5
CI	323.9	52.7	18.3	8.9	5.0	3.1	2.1

Table 3. Median of the eccentricity residuals. The table lists the results against the SNR for the coherent integration IOD and all the algorithms that perform the fit on the measurements.

	0 dB	5 dB	10 dB	15 dB	20 dB	25 dB	30 dB
KJ	0.0841	0.0447	0.0236	0.0129	0.0076	0.0054	0.0048
HGf	0.0842	0.0439	0.0232	0.0119	0.0061	0.0031	0.0017
HGGf	0.0841	0.0440	0.0231	0.0119	0.0060	0.0031	0.0017
HGGRRf	0.4430	0.2508	0.1385	0.0746	0.0396	0.0207	0.0103
TBf	0.2356	0.1386	0.0799	0.0463	0.0266	0.0145	0.0082
CI	0.1091	0.0153	0.0040	0.0016	0.0009	0.0005	0.0004

Table 4. Median of the inclination residuals. The table lists the results in deg *against the SNR for the coherent integration IOD and all the algorithms that perform the fit on the measurements.*

	0 dB	5 dB	10 dB	15 dB	20 dB	25 dB	30 dB
KJ	3.24	1.81	1.08	0.69	0.54	0.50	0.51
HGf	3.23	1.81	1.02	0.57	0.32	0.18	0.10
HGGf	3.24	1.81	1.02	0.57	0.32	0.18	0.10
HGGRRf	3.26	1.81	1.02	0.57	0.32	0.18	0.10
TBf	3.20	1.82	1.04	0.63	0.42	0.34	0.32
CI	9.17	2.33	0.91	0.43	0.23	0.13	0.07

Table 5. Median of the true longitude residuals. The table lists the results in deg *against the SNR for the coherent integration IOD and all the algorithms that perform the fit on the measurements.*

	0 dB	5 dB	10 dB	15 dB	20 dB	25 dB	30 dB
KJ	4.02	2.34	1.38	0.88	0.67	0.61	0.63
HGf	3.98	2.24	1.25	0.70	0.40	0.22	0.12
HGGf	3.98	2.24	1.25	0.70	0.40	0.22	0.12
HGGRRf	4.06	2.24	1.25	0.70	0.40	0.22	0.12
TBf	4.08	2.28	1.31	0.79	0.53	0.42	0.39
CI	11.83	2.95	1.14	0.54	0.28	0.16	0.09

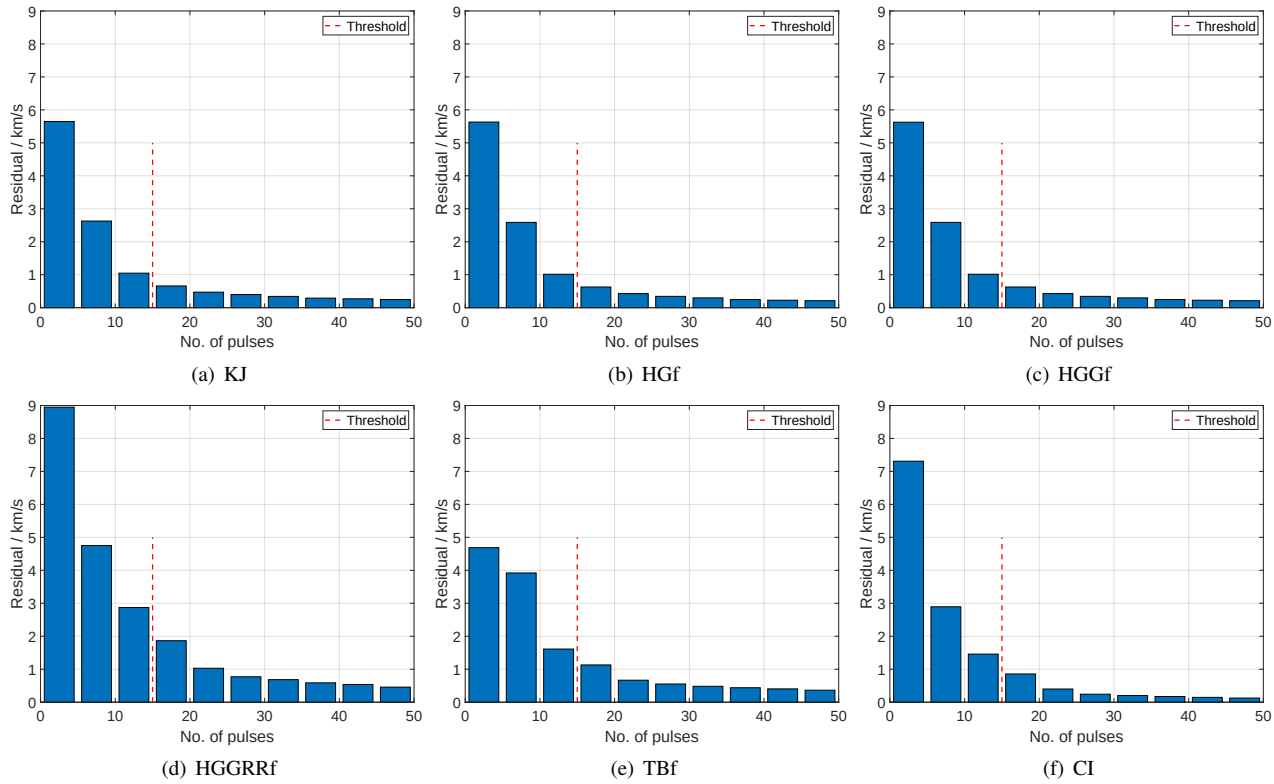

Figure 7. Mean of the norm of the velocity vector difference obtained with an SNR of 15 dB *for the coherent integration IOD and all the algorithms that perform the fit on the measurements. The figures present the residuals in* km/s *against the number of pulses associated with the simulated beam crossings (up to a maximum of 50 pulses). The dashed red line represents the threshold of 15 pulses.*

mately a plateau for all the considered techniques. The threshold of 15 pulses, chosen for the previous investigation, is included as well in the plots as a vertical dashed red line.

For all the IOD methods, as expected, a higher number of pulses leads to smaller residuals. Such gain is especially visible for very low numbers of pulses. Once more, almost the exact same behavior can be observed for HGf and HGGf.

For the first cluster, TBf is the algorithm giving the best accuracy. Then, up to a number of 20 pulses, HGf and HGGf become the favorable methods. Finally, with higher numbers of pulses, this result is overturned by CI. The IOD solutions obtained by all the algorithms in correspondence with a number of pulses below 10, do not bring any valuable information, since the minimum mean error is in the order of 2.5 km/s (i.e., around the 35% of the standardly assumed LEO regime velocity vector norm of 7 km/s).

Analogous plots were derived for the other considered SNR values as well (here not presented). The observed trends were the same as the ones depicted in Figure 7, with a shift of the residuals towards higher or lower values, according to the corresponding SNR (a higher SNR value led to smaller residuals and vice versa).

5. CONCLUSIONS

In this paper we investigated the accuracy of several IOD techniques applied to simulated noisy BPE data. The idea behind the analysis was to understand whether or not, for calibrating the space debris population models, the output of such techniques could be a beneficial addition to the detection list already provided by Fraunhofer FHR after a BPE.

We presented the accuracy reached by the IOD algorithms in terms of position and velocity vectors as well as in terms of orbital parameters, with respect to different SNR values for all the beam crossings with a visibility time of at least 0.5 s. It is important to underline again that such performances correspond only to an upper bound since, in this investigation, we assumed a constant value for the SNR along each pass, neglecting the RCS variations over time, the antenna pattern modulation and the phase decorrelation effects. As anticipated in Section 1, all these features, occurring with real observations, introduce a series of problems (e.g., discontinuities in the target detection over time) leading to a degradation of the actual IOD performances. Additionally, another reason for considering this analysis as an upper bound is the introduction of the minimum number of pulses constraint used in Section 4.1. Indeed, we demonstrated that, removing this constraint, the accuracy of all the different

techniques was negatively affected.
We showed the importance of performing an initial fit on the radar measurements to reduce the oscillations introduced by the noise. Moreover, since for some IOD techniques, only few observation vectors are taken as input, the fit represents a quick way to take into consideration the information included in all the other pulses provided by the radar as well.
The processing through the IOD methods of the data obtained after the realization of a BPE, is an offline operation. Therefore, the computational load is not a discriminating factor. However, concerning this facet, there is a great difference between the selected algorithms. Specifically, CI requires the longest time, followed by HGG and HGGRR, while all the other techniques (KJ, HG and TB) need considerably less time. CI is the most time-consuming method because it is based on two steps, a computationally intensive filtering process [9] and the actual IOD. The realization of the initial fit on the measurements does not alter considerably the computational cost, so it can be neglected in this context.
In all the figures and tables shown, we saw that HGf and HGGf give almost exactly the same residuals. Indeed the two algorithms are practically identical. The main difference is in the number of observation vectors taken as input. However, when a fit is performed on the measurements to force these latter to follow a linear trend, using more observation vectors does not bring any new information. Indeed, in such cases, the measurement dynamics is already well-captured by the three pulses considered within the original HGf algorithm.
CI is the only technique able to improve the estimate of the position vector. This quantity is directly determined from the measurements of range, azimuth and elevation coming from the radar. This is why all the other algorithms reach always the same accuracy in terms of position estimate. The improvement introduced with CI is due to the fact that, within the coherent processing, the filtering step is able to enhance the accuracy of the measurements of range, azimuth and elevation themselves [9]. A possibility for the future, would be to feed the more accurate filtered measurements, obtained through the first step of CI, to the other selected IOD techniques as well and, then, to compare again their performances.
Another important consideration is that, so far, as mentioned in Section 2, no radar performance model was included in the simulation to compute the detection probability. For this reason, we included in the investigation also the values of 0 dB and 5 dB for the SNR. However, a common detection threshold for the radar is in the order of 10-15 dB. In a real experiment, especially focused on small objects (as the majority of the space debris is), it could be too optimistic to expect to be able to distinguish the signal back-scattered from such objects in correspondence with an SNR of 0 dB or 5 dB. Having this in mind, we can say that for all the results shown, if we fix a lower bound of 10 dB for the SNR, the CI algorithm is always the IOD technique performing best. Thus, these first findings highlight the potential of performing a coherent processing of the radar measurements also in terms of IOD applications [9].
To answer the question at the basis of the paper, the application of an IOD technique to BPE data seems to be able to add some valuable information, at least in bounding the orbital elements. The advantages brought by the use of such techniques are certainly strongly dependent on the accuracy of the measurements obtained from the radar (i.e., on the SNR), as well as on the length of the observed pass and, therefore, should be evaluated on a case by case basis.

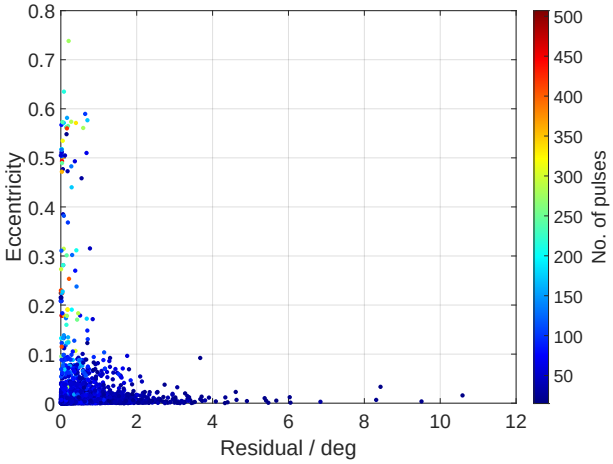

Figure 8. Inclination residuals obtained with an SNR of 15 dB *for CI. The residuals are plotted in* deg *against the TLE eccentricity for the 3018 simulated beam crossings. The colorbar indicates the associated number of pulses.*

So far, we focused on a single BPE configuration, but as shown in [6], to different beam pointing directions correspond different radar parameter trends as well. As a future work, it would be interesting to perform a similar analysis with other BPE configurations.
Figure 6 showed that the various algorithms perform differently with respect to the three main directions of the RSW reference frame. It could be an idea to combine the outputs of several algorithms together to try to enhance the final accuracy.
Lastly, another possible investigation for the future would be to focus on a single technique and to study how its accuracy changes according to the orbital geometry of the beam crossing object. As an example, Figure 8 shows, for each of the 2960 passes with at least 15 pulses, the inclination residuals obtained with an SNR of 15 dB using CI, against the TLE eccentricity and the associated number of pulses (indicated in the colorbar).

ACKNOWLEDGMENTS

Part of this work was supported by ESA-ESOC (Contract No. 4000127260/19/D/SR).

REFERENCES

1. Kessler D.J., Cour-Palais B.G., (1978). Collision frequency of artificial satellites: the creation of a debris

belt. *Journal of Geophysical Research*, **83**(A6), 2637–2646

2. ESA Space Debris User Portal. Space Environment Statistics. *https://sdup.esoc.esa.int/discosweb/statistics* (accessed on 10.03.2021)

3. Aida S., Patzelt T., Leushacke L., Kirschner M., Kiehling R., (2009). Monitoring and mitigation of close proximities in Low Earth Orbit. *21st ISSFD Conference, Toulouse, France*

4. Bohannon G.E., Young N., (1993). Debris size estimation using average RCS measurements. *Report No. 930781-BE-2247, XonTech, Inc.*

5. Budoni M., Carloni C., Cerutti-Maori D., Maouloud I.O., Rosebrock J., (2020). Investigation of the radar parameter subspace measured with the TIRA system for selected beam-park configurations and its relations with the Keplerian parameter space. *Intermediate report 1, ESA Contract No. 4000127260/19/D/SR*

6. Budoni M., Carloni C., Cerutti-Maori D., Maouloud I.O., Rosebrock J., Flegel S.K., Lemmens S., (2020). Investigation of the radar parameter subspace for different beam-park simulations with the TIRA system. *71st IAC Conference, Cyberspace edition*

7. SAIC. *https://www.space-track.org* (accessed on 12.12.2019).

8. Vallado D.A., Crawford P., (2008). SGP4 Orbit Determination. *AIAA/AAS Astrodynamics Specialist Conference and Exhibit, Honolulu, Hawaii*

9. Cerutti-Maori D., Budoni M., Carloni C., Klare J., Maouloud I.O., Rosebrock J., (2021). A novel high-precision observation mode for the Tracking and Imaging Radar TIRA - principle and performance evaluation *8th European Conference on Space Debris, Darmstadt, Germany*

10. Budoni M., Carloni C., Cerutti-Maori D., Maouloud I.O., Rosebrock J., (2020). Investigation and comparison of the performance of selected IOD techniques for BPE with the TIRA system. *Intermediate report for WP5300, ESA Contract No. 4000127260/19/D/SR*

11. Kaiser H., Jehn R., (1996). Determination of rough orbital elements from radar data in beam-park mode. *ESA-ESOC MAS working paper no. 377*

12. Herrick S., (1971). *Astrodynamics: orbit determination, space navigation, celestial mechanics (Vol. I)*. Van Nostrand Reinhold Co.

13. Gibbs J., (1889). On the determination of elliptic orbits from three complete observations *Memoires National Academy of Science*, **4**(2), 79–104

14. Taff L.G., Hall D.L., (1977). The use of angles and angular rates, I: Initial orbit determination. *Celestial Mechanics*, **16**, 481–488

15. Milani A., Gronchi G.F., (2009). *Theory of orbit determination*. Cambridge university Press

16. Gronchi G.F., Dimare L., Milani A., (2010). Orbit determination with the two-body integrals. *Celestial Mechanics and Dynamical Astronomy*, **107**, 299–318

17. Gronchi G.F., Farnocchia D., Dimare L., (2011). Orbit determination with the two-body integrals. II. *Celestial Mechanics and Dynamical Astronomy*, **110**, 257–270

18. Gronchi G.F., Baù G., Marò S., (2015). Orbit determination with the two-body integrals: III. *Celestial Mechanics and Dynamical Astronomy*, **123**, 105–122

19. Carloni C., Budoni M., Cerutti-Maori D., Rosebrock J., (2021). Performance analysis of tracking filters according to input data processing *8th European Conference on Space Debris, Darmstadt, Germany*

20. Vallado D.A., (2013). *Fundamentals of Astrodynamics and Applications*, Space Technology Library, ed. 4 (p. 155)